

# **Implementing 3D Imaging in Single Molecule Localization Microscopy with Astigmatism**

Master's thesis

Student: Marten Pärj

Student code: 163065YAFM

Supervisor: Martin Laasmaa, assistant professor, TalTech

Study program: YAFM02/14 - Applied Physics

Tallinn 2025

## DECLARATION

I hereby declare that I have compiled this paper independently, and all sources, important viewpoints, and data by other authors have been properly referenced. This paper has not been previously submitted for assessment.

Author: Marten Pärt

[Signed digitally 21.05.2025]

The thesis complies with the requirements for Master's theses.

Supervisor: Martin Laasmaa

[Signed digitally 21.05.2025]

# Table of contents

<b>Abbreviations</b>	<b>5</b>
<b>Introduction</b>	<b>6</b>
<b>1 Theory</b>	<b>7</b>
1.1 Overview of resolution in microscopy . . . . .	7
1.1.1 Point spread function and the Airy pattern . . . . .	8
1.2 Super-resolution microscopy . . . . .	10
1.2.1 Single-molecule localization microscopy . . . . .	10
1.2.2 Structured illumination microscopy . . . . .	11
1.2.3 Stimulated emission depletion . . . . .	11
1.3 (Direct) Stochastic optical reconstruction microscopy . . . . .	11
1.3.1 Dyes and blinking behaviour . . . . .	12
1.3.2 2D Localization . . . . .	13
1.3.3 3D Localization . . . . .	14
1.4 Total internal reflection fluorescence . . . . .	15
<b>2 Task description</b>	<b>16</b>
<b>3 Consideration of potential approaches</b>	<b>18</b>
3.1 Phase mask . . . . .	18
3.2 Phase ramp . . . . .	18
3.3 Astigmatism-based . . . . .	19
<b>4 Methodology</b>	<b>20</b>
4.1 Cylindrical lens placement . . . . .	20
4.2 Imaging z-stacks . . . . .	22
4.3 Post-imaging data processing . . . . .	23
<b>5 Results</b>	<b>27</b>
5.1 Point spread function shapes . . . . .	27
5.2 Elliptical Gaussian function fitting at lowered laser light . . . . .	30
<b>6 Discussion</b>	<b>35</b>

<b>7 Acknowledgments</b>	<b>36</b>
<b>References</b>	<b>39</b>
<b>Appendices</b>	<b>41</b>
Appendix 1 - Non-exclusive licence for reproduction and publication of a graduation thesis	41

## **Abbreviations**

(d)STORM - (direct) Stochastic Optical Reconstruction Microscopy

TIRF - Total Internal Reflection Fluorescence

PSF - Point Spread Function

SIM - Structured Illumination Microscopy

STED - Stimulated Emission Depletion

SMLM - Single Molecule Localization Microscopy

PALM - Photoactivated Localization Microscopy

LQ - Least Squares

MLE - Maximum Likelihood Estimation

SLM - Spatial Light Modulator

SNR - Signal-to-Noise Ratio

## Introduction

For studying biological systems, high resolution imaging is crucial. With many molecules measuring on the order of single nanometers in size, high resolution is needed to better understand events taking place at such scale. This level of detail can, for instance, allow observation of protein-protein interactions, more detailed intracellular structures and intracellular trafficking [1].

Due to the diffraction limit imposed by the objective, conventional light microscopy is restricted to ~200 nm lateral resolution. Although other types of imaging methods, such as electron microscopy or cryo-EM, offer higher resolutions, they often come with requirements for the sample (e.g., vacuum environment, ultra thin slicing or freezing temperatures). These requirements are however incompatible for some types of samples or make the sample preparation overly costly and/or time consuming. For these reasons, light microscopes remain the preferred tool for biological samples.

Over the last 3 decades, super-resolution techniques have been developed to help light microscopes overcome the diffraction limit. One of those is called direct stochastic optical reconstruction microscopy (dSTORM), which achieves localization of individual fluorophores at resolution near 20 nm. Total internal reflection fluorescence (TIRF) is often used in conjunction with dSTORM to increase signal-to-noise ratio (SNR).

While dSTORM allows sub-diffraction limit lateral resolution, it does not reveal the positions of the fluorophores in the axial direction. Taking multiple dSTORM images at different focal planes to reconstruct a 3D image is not practical as well, due to photobleaching, long acquisition times and complexity of precise alignment across z-stacks. The shape of the point-spread function (PSF) is intentionally modified to introduce z-axis information. Most popular existing approaches to this are through the use of cylindrical lenses or phase masks, which distort the PSF in a z-dependent manner. This enables the acquisition of the z-axis location information of the fluorophores and the reconstruction of a 3D image.

This thesis presents a practical approach to modifying an existing microscope setup, already used to acquire TIRF dSTORM images, with a cylindrical lens to achieve 3D imaging capabilities. Motivated by the lack of clear step-by-step guidance in academic literature for implementing such modifications, this work demonstrates a cost-effective and robust method for enabling axial localization through astigmatism-based PSF shaping.

# 1 Theory

## 1.1 Overview of resolution in microscopy

Through manipulation of light with the help of lenses, light microscopy allows visualization of objects at microscopic scales. Light is shone through or reflected off a sample, manipulated with optical components and then ultimately focused to form an image on either a camera chip or a human eye at an eyepiece. Depending on the need, there are usually multiple optical components in a microscope setup - various lenses, filters, mirrors, prisms, diaphragms... The behaviour of light with interaction of these components is mainly governed by the principles of wave optics, particularly diffraction and interference.

The visualization of objects with conventional light microscopes is only possible up to a certain level of resolution. When light passes through the rear aperture of the objective, there is a diffraction pattern created in the light wavefront. This diffraction pattern convolutes the final image, reducing its resolution. This fundamental resolution barrier due to diffraction was first mentioned by Ernst Abbe in 1873 and is now called the Abbe diffraction limit. [2] It states that the smallest resolvable feature with an light microscope is given by the following formula:

$$d = \frac{\lambda}{2n \sin \theta} = \frac{\lambda}{2NA} \quad (1)$$

where  $d$  is size of the smallest resolvable feature,  $\lambda$  is the wavelength of observed light,  $n$  is the refractive index of the medium and  $\theta$  is the half angle over which the objective can collect light from the sample. The formula can also be written with the objective's numerical aperture  $NA = n \cdot \sin(\theta)$ .

To see as much detail as possible with conventional light microscopes, we are stuck with this limit. We can deduce from this formula that in order to increase the resolution, one way would be to decrease the wavelength of collected light. But using shorter wavelength electromagnetic waves is often not a viable option, as they will easily damage observed biological samples and require more specialized (expensive) equipment. Another way to theoretically increase the resolution seems to be to increase the numerical aperture. But this is also already at the limit of possibilities. The theoretical maximum of  $\sin(\theta)$  is 1 and immersion mediums with a refraction index above ~1.5 are impractical for biological samples.

Using a common numerical aperture value of 1.5 and red light wavelength of 650 nm, the resulting size for the smallest resolvable feature according to Abbe diffraction limit would be ~217 nm. This is why ~200 nm is considered the approximate resolution limit in light microscopy.

### 1.1.1 Point spread function and the Airy pattern

Due to diffraction, every point imaged with a light microscope will be blurred in a way that is distinct to the given optical system. This function is called the point spread function. It depends on:

- the numerical aperture of the objective lens,
- the wavelength of observed light,
- the refractive index of the medium between the sample and the objective
- and on any optical components causing aberrations or some deliberate light manipulation.

This blurring does not happen only in 2 dimensions, but in 3. Knowing the exact shape of the PSF of one's optical system is sometimes needed for post-imaging picture analysis, allowing to increase resolution through computational methods. With commercial microscopes, the PSF is sometimes pre-calibrated and given to the client. If this is not available or a microscope setup is modified by the user, changing the PSF along with it, there are other options of obtaining the PSF. One can, for example, measure the PSF experimentally. This is done by imaging a sufficiently small fluorescent object, imitating an ideal point source light emitter. To get the full 3D PSF, one needs to image the object at various focal lengths and combine the data with a software. This method may be time consuming and requires careful calibration, but it captures the real PSF of ones microscope, including any aberrations. The PSF can also be obtained by approximation with a theoretical model. In its ideal form, without any aberration or refractive index mismatch, the PSF can be derived through mathematics. This idealized version is called the Airy pattern. The Airy pattern describes the intensity distribution of light that is diffracted by a circular aperture. In the case of a microscope, this circular aperture is the rear aperture of the objective. Starting from the Fraunhofer diffraction equation in polar coordinates and using a circular aperture of radius  $a$ , the complex amplitude  $U$  at a point  $P$  far from the aperture is given by:

$$U(P) = C \int_0^{2\pi} \int_0^a e^{-ik\rho w \cos(\theta-\psi)} \rho d\rho d\theta \quad (2)$$

with  $\rho$  and  $\theta$  being polar coordinates of the aperture,  $w = \sqrt{p^2 + q^2}$  being the radial coordinate in the diffraction pattern and  $\psi$  the angle between  $w$  and the  $x$ -axis.

Using the zeroth order Bessel function of the first kind in integral form:

$$J_0(z) = \frac{1}{2\pi} \int_0^{2\pi} e^{iz \cos \theta} d\theta \quad (3)$$

and substituting  $z = k\rho w$ , we get:

$$U(P) = 2\pi C \int_0^a J_0(k\rho w) \rho d\rho \quad (4)$$

Using the Bessel function integral identity:

$$\int_0^x x' J_0(x') dx' = x J_1(x) \quad (5)$$

and substituting  $x = kaw$ , we get:

$$U(P) = CD \left[ \frac{2J_1(kaw)}{kaw} \right] \quad (6)$$

where  $D = \pi a^2$  is the aperture area. Defining  $|CD|^2$  as the intensity at the center of the diffraction patten, where  $w = 0$ , and knowing intensity is proportional to the square of the magnitude  $I(P) = |U(P)|^2$ , we arrive to the Airy pattern intensity profile [3]:

$$I(P) = I_0 \left[ \frac{2J_1(kaw)}{kaw} \right]^2 \quad (7)$$

Plotting this intensity profile radially outwards from the center we get Figure 1.

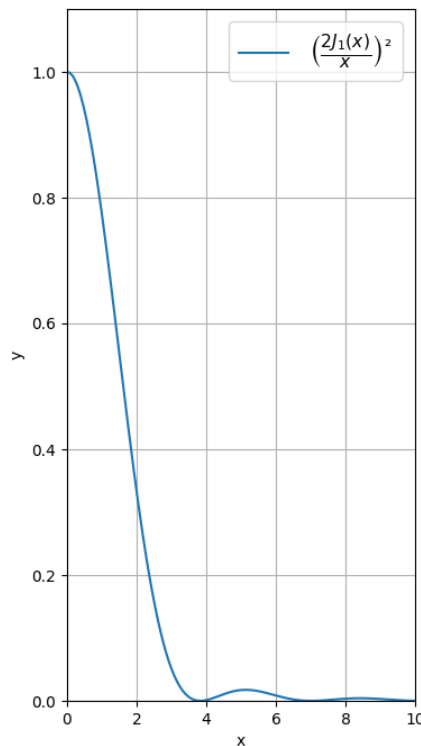


**Figure 1:** Intensity profile of the Airy pattern. Vertical axis representing normalized light intensity and horizontal axis representing radial distance from the center of the pattern in arbitrary distance units.

The pattern consists of an intense central maximum, called the Airy disk, and weaker concentric rings around it, called the Airy rings. Plotting this out in 2D and softening the intensity values by a power

of 0.3 to make the rings more visible, we can finally see the Airy pattern on Figure 2.

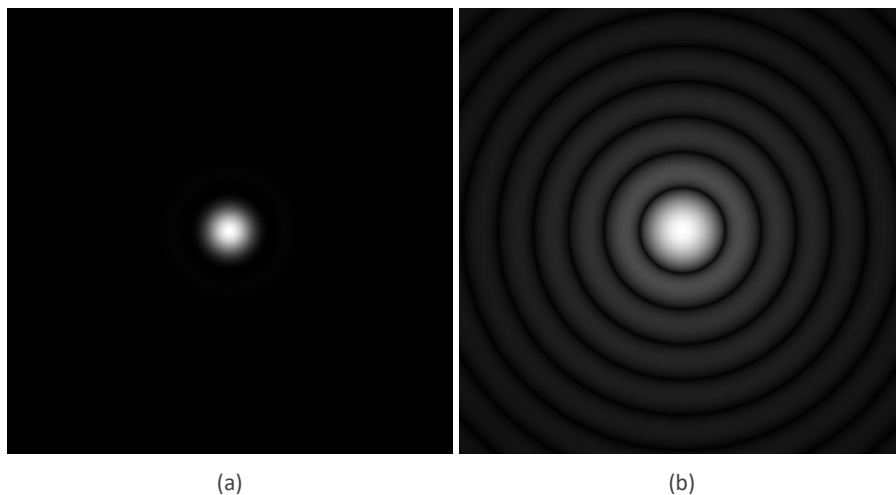


**Figure 2:** Simulated 2D Airy patterns. Scale is shown in arbitrary distance units. No gamma correction is applied on Figure (a). Intensity values on Figure (b) are gamma-corrected with an exponent of 0.3 to make the low intensity concentric Airy rings more visible. `matplotlib`

## 1.2 Super-resolution microscopy

Considering biological molecules can be as small as in the range of single digit nanometers, a resolution limit of  $\sim 200$  nm is not good enough to observe all possible events happening in a cell. For greater study of biological mechanisms, better resolution is needed. Over a century after Abbe diffraction limit was termed, techniques that allowed light microscopes to overcome the limit started to emerge. By now there are a numerous amount of them, each tackling the problem at a slightly different angle and lacking a single common denominator. They are achieved through combinations of optical physics, fluorescence chemistry, and computational algorithms. Such techniques are named under the umbrella term: Super-resolution microscopy. These methods enable light microscopy imaging at resolution down to tens of nanometers, having already enabled research into biological systems at a scale that was previously impossible.

### 1.2.1 Single-molecule localization microscopy

Single-Molecule Localization Microscopy (SMLM) is a group of super-resolution microscopy techniques. These techniques rely on capturing the isolated PSFs of individual fluorescent molecules. If a PSF is observed individually without any neighbouring signal to disturb its shape, the real location of the molecule corresponding to this PSF can be more accurately inferred. This requires precise knowledge of the shape of the PSF your given microscope and imaging setup produces. The localization precision achieved with these methods is on the order of tens of nanometers. More popular SMLM methods are STORM/dSTORM, PALM and DNA-PAINT.

### **1.2.2 Structured illumination microscopy**

Structured illumination microscopy (SIM) is a super-resolution microscopy technique that takes advantage of the moiré effect. [4] When two periodic patterns of approximately similar frequency are overlapped, they produce a new pattern of a lower frequency than both of the original ones. If the frequency of one of the original patterns is known and the resulting pattern can also be observed, then it is possible to calculate the frequency of the second pattern.

In SIM, the spatial distribution of the excitation light is modified to have a repeating pattern with the periodicity near the diffraction limit. The pattern could be a simple sinusoidal striped pattern or something more complex. This structured light pattern can be achieved through inserting an additional element into the light path (e.g., diffraction grating, spatial light modulator). When this structured light interacts with the sample's features, it creates a moiré effect, shifting high frequency information from the sample down to a detectable frequency. Multiple images are taken with the pattern of the structured light rotated to different angles and shifted to different phases. Through computational algorithms an image of the sample is reconstructed and a resolution improvement of ~2x better than the diffraction limit is achieved. Although SIM offers only marginal improvement over conventional light microscopy, it is still widely used, mainly because of its high speed and ease of use.

### **1.2.3 Stimulated emission depletion**

Stimulated Emission Depletion (STED) microscopy, developed in 1994 [5], is a super-resolution microscopy technique using two laser beams to precisely control the location on the sample where fluorescence takes place. It uses an excitation laser to excite the fluorescent molecules and another laser of a slightly longer wavelength, the depletion laser, which forces excited fluorophores back to their ground state in a determined manner. The imaging usually requires a scanning process, where the sample is illuminated by the lasers step-by-step in a grid fashion. The excitation laser excites fluorophores in a small region at a time and the depletion laser concurrently stimulates photon emission at the same target location except a small region in the middle, leaving fluorophores there in an excited state. The photons stimulated to emit are of the same wavelength as the excitation laser and thus easily filtered out, while the fluorophores left in their excited state will return to their ground state through fluorescence. Fluorescence photons will be of a different wavelength and not filtered out. By compiling the precise locations of fluorescent molecules at each step, it becomes possible to reconstruct an image at a sub-diffraction-limited resolution.

## **1.3 (Direct) Stochastic optical reconstruction microscopy**

Stochastic Optical Reconstruction Microscopy (STORM) and direct Stochastic Optical Reconstruction Microscopy (dSTORM) are closely related SMLM techniques. They rely on labeling specific molecules within a cell with special dyes that, upon illumination with the excitation laser, will not exhibit a continuous emission signal, but rather will blink stochastically. Because the fluorophores do not all

emit a signal simultaneously, rather than taking one image, one has to take a video. On that video one can see different fluorophores emitting a signal at different frames. This means the PSFs are not overlapping each other and only a sparse subset of PSFs can be observed at any given frame. Knowing the PSF shape of the used microscope allows one to reconstruct the location of molecular positions through fitting. This yields a localization precision down to ~10-20 nm in the x-y plane.

### 1.3.1 Dyes and blinking behaviour

The blinking process of STORM/dSTORM relies on photoswitching of dyes to alternate them being in bright and dark states. This blinking is shown on Figure 3.

In the regular STORM method, a pair of dyes is used: an activator dye and a reporter dye. One activation laser is used to excite the activator dye. This dye can stochastically transfer energy to the reporter dye, activating it from a non-fluorescent (dark) state into an active state. A second laser, the excitation laser, is used to excite the active reporter fluorophore to emit fluorescence and switch back to the non-fluorescent state, ready to be reactivated by the activation dye again. Since the energy transfer from the activation dye to the reporter dye is stochastic, the reporter dye fluorophores will not all emit simultaneously, but rather blink stochastically. Commonly used activator dyes are Alexa Fluor 405, Cy2 and Cy3 and reporter dyes are Alexa Fluor 647 and Cy5. [6] [7] [8]

In dSTORM, blinking behaviour is achieved chemically and does not rely on an activator-reporter dye pair, which makes the method more straightforward. A special chemical solution, called the switching buffer or redox buffer, needs to be added to the sample. An excitation laser is still used on the sample to push the fluorophores from the ground state ( $S_0$ ) to an excited state ( $S_1$ ) and on most occurrences they relax back to the ground state by emitting a photon. However, the buffer resists the normal transfer back from the excited state to the ground state. Because of the buffer, there is a low but functionally significant probability for the fluorophore to move into a metastable non-fluorescent state ( $T_1$ ) instead. The fluorophore can stay in this state for up to several seconds and will return to the ground state ( $S_0$ ) in a stochastic time manner. Once back in the ground state, it is ready to be excited by the laser again. Due to the relatively long time a fluorophore will stay in the metastable dark state ( $T_1$ ), even though the likelihood of it entering the state at any given excitation event is low, at any given time during an imaging, most fluorophores will reside in the metastable dark state. The stochastic nature of the fluorophores coming out of the metastable state results in the blinking of the fluorophores. Although most fluorescent dyes can be used in dSTORM, Alexa Fluor 647 [9] is seen as one of the best suited for it and thus most commonly used. It has to be mentioned that the switching buffer can be different for different dyes. Thus, when doing multicolor labeling, one must find dyes that perform well in the same redox buffer. For example, while Alexa 647 blinks well in a compound called Vectashield when using it together with Alexa 555, the redox buffer needs to be replaced with a mixture of Vectashield and Tris-Glycerol. [10]

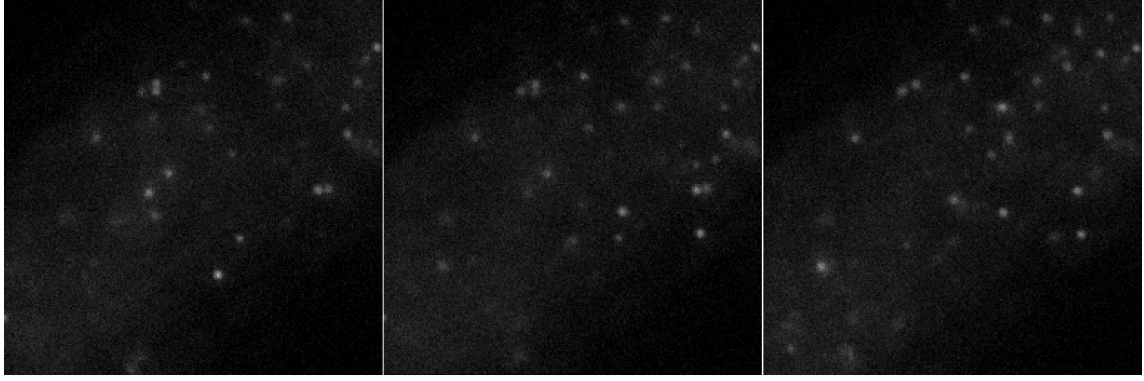


**Figure 3:** Individual consecutive frames from a dSTORM imaging, showing the blinking behaviour of fluorophores. Image at a scale of 256x256 pixels with 70 nm per pixel (17.92x17.92  $\mu\text{m}$ ). Imaging parameters: Alexa Fluor 647, 50 ms exposure time per frame, 100x objective with an NA of 1.45, imaging buffer of 20% Vectashield and 80% Tris-Glycerol, mitochondrial calcium uniporter proteins dyed in a cardiomyocyte. Images recorded by Irina Česnokova.

### 1.3.2 2D Localization

To localize the positions of the fluorophores, their individual PSFs are fitted with a two-dimensional Gaussian function:

$$I(x, y) = I_0 \cdot \exp\left(-\frac{(x - x_0)^2 + (y - y_0)^2}{2s^2}\right) + b \quad (8)$$

where  $I_0$  is the peak intensity,  $(x_0, y_0)$  is the center (location of the fluorophore),  $s$  is the standard deviation of the PSF width and  $b$  is background intensity.

The fitting is usually done via least-squares method (LQ):

$$\chi^2 = \sum_{x,y} [I_{\text{data}}(x, y) - I_{\text{model}}(x, y)]^2 \quad (9)$$

or a maximum likelihood estimation (MLE):

$$\mathcal{L} = \sum_{x,y} [I_{\text{data}}(x, y) \cdot \ln I_{\text{model}}(x, y) - I_{\text{model}}(x, y) - \ln (I_{\text{data}}(x, y)!)] \quad (10)$$

A practical estimation for the localization uncertainty can be given [11] with the equation:

$$\sigma_{\text{loc}}^2 \approx \frac{s^2 + \frac{a^2}{12}}{N} + \frac{4\sqrt{\pi} s^3 b^2}{aN^2} \quad (11)$$

where  $a$  is the pixel size and  $N$  is the number of detected photons in a PSF. This equation shows

that localization uncertainty decreases with a higher detected photon count and a lower background noise.

### 1.3.3 3D Localization

As seen from the previous chapter, fitting PSFs with a Gaussian function does not reveal any z-axis location information. All the fluorophores are localized only by their x- and y- coordinates. Since intracellular structures are rarely only 2-dimensional, there is clear merit from trying to extract z-axis location data from the PSF as well. There have been multiple methods trying to achieve that. The main approaches involve modifying the 3D shape of the PSF. This is called PSF engineering.

The most common PSF engineering method, also used in this thesis, is with the help of astigmatism. Adding an optical element such as a cylindrical lens [12] or an electrically controllable deformable mirror [13] to the optical path of the microscope introduces astigmatism to the system. Fluorophores that do not lie directly in the focal plane of the microscope will have their PSFs elongated. Whether a PSF is elongated in the x-axis or the y-axis will depend on which side of the focal plane the fluorophore is situated. The magnitude of the elongation is dependent on the distance of the fluorophore from the focal plane, with more out of focus fluorophores exhibiting stronger astigmatism. By using an elliptical Gaussian function to fit the PSFs and observing the ellipticity, it is possible to determine the distance and direction of the fluorophore from the focal plane in the z-axis. The elliptical Gaussian function is usually given in the following form:

$$I(x, y) = I_0 \cdot \exp \left( - \left[ \frac{(x - x_0)^2}{2s_x^2} + \frac{(y - y_0)^2}{2s_y^2} \right] \right) + b \quad (12)$$

where  $I_0$  is the peak intensity,  $(x_0, y_0)$  is the center (location of the fluorophore),  $s_x, s_y$  are the standard deviations of the PSF width/height and  $b$  is background intensity.

Another PSF engineering method, that is gaining popularity, is the use of phase masks. Phase masks are optical elements that shift the phase of light in a spatially varied pattern (Figure 4). These can be lithographically manufactured plates that let light through or devices that reflect light in a precise manner, such as deformable mirrors or spatial light modulators (SLMs). By placing a phase mask in the Fourier plane of a microscope's optical path, one can modulate the 3D shape of a PSF with high precision, causing systematic changes that depend on the z-axis location of the fluorophore (Figure 5). The localization of these PSFs are more complex than with a single Gaussian function and often require the help of artificial neural networks. [14]

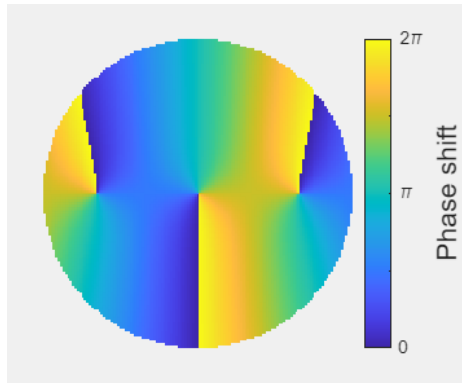


**Figure 4:** Phase profile of a double helix phase mask. Scale is shown in arbitrary distance units. PSF simulation application [15] on MATLAB used.

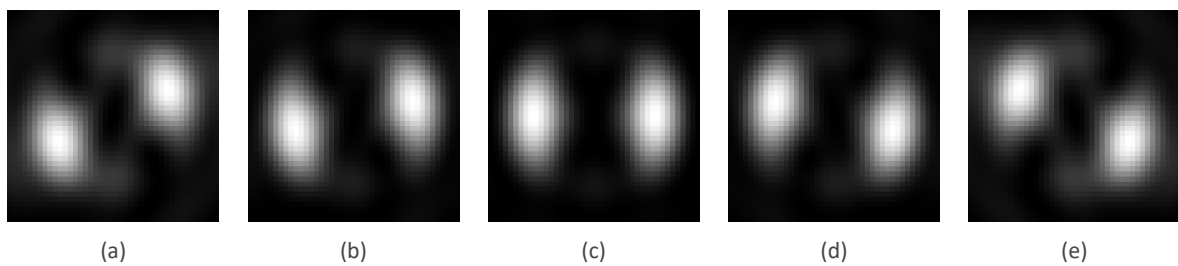


**Figure 5:** Simulated PSFs that are achieved via a double helix phase mask on Fig. 3. The images show the two lobes rotating with different chosen focus depths. Parameters used: emission wavelength of 680 nm; NA of 0.7; photon count 50000. Scale is shown in arbitrary distance units. The defocus is set to (a) -1000 nm, (b) -500 nm, (c) 0 nm, (d) +500 nm, (e) +1000 nm. PSF simulation application, MATLAB

## 1.4 Total internal reflection fluorescence

Light propagating through a high refractive index medium (e.g., glass) encountering an interface with a lower refractive index medium (e.g., water) will be fully reflected back into first medium if the incident angle is equal or above a critical angle. This is called total internal reflection. In such cases, while no light will escape into the lower refractive index medium, there will be non-propagating evanescent waves generated in it. The intensity of these waves will exponentially decay with the distance from the medium change. These evanescent waves typically have a penetration depth on the order of tens to hundreds of nanometers.

This phenomenon is sometimes used in microscopy. By directing coherent light onto the coverslip or the slide at an angle exceeding the critical angle between the glass and the sample medium, evanescent waves are created within the sample only very near the glass surface. This allows for selective excitation of fluorophores that are located close to the glass, significantly reducing background fluorescence created by fluorophores deeper in the sample and by this drastically improving the signal-to-noise ratio in imaging. This method is often referred to total internal reflection fluorescence (TIRF) microscopy. [16]

## 2 Task description

The central aim of the work in this thesis was to modify an existing microscope, that was already capable of being used with dSTORM imaging, to optionally also support 3D dSTORM imaging. The microscope in question was the TILL iMIC (Figure 6), originally manufactured by TILL Photonics GmbH (a company later bought by FEI Company - Field Electron and Ion Company, which in turn is now a subsidiary of Thermo Fisher Scientific).

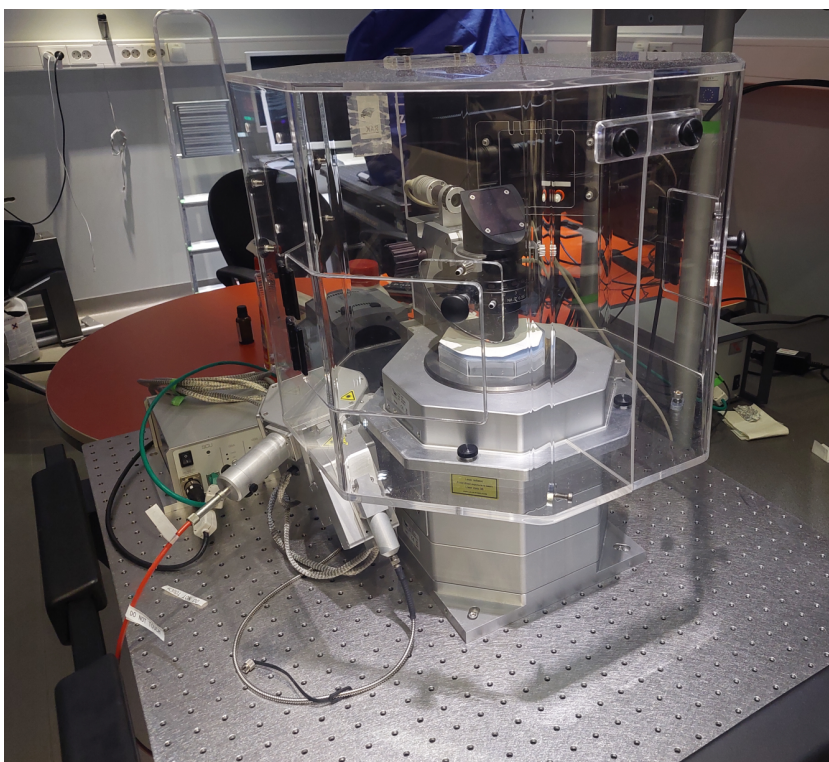


Figure 6: TILL iMIC microscope mounted on a vibration isolation table.

Relevant equipment the optical system already had: an Andor Technology iXonEM+ EMCCD camera, a laser with 640 nm central wavelength, an integrated Zeiss tube lens, an external Rodenstock relay lens and a varied choice of objectives and filters. The optical system was mounted on a vibration isolation table, which had a limited amount of space for extra equipment. Software used to control both the microscope stage and the camera was `Live Acquisition` from TILL Photonics.

To leave the option open for the microscope to be used for other imaging methods than only 3D dSTORM, the added modification had to be mounted in a manner that could be easily removed and reapplied when needed. The modification would also ideally be calibrated for an optimal combination of x-, y- and z-localization precision balance.

Given that Alexa Fluor 647 is the most used dye in dSTORM imaging and is also the primary used dye when imaging is done with this microscope, any added optical element should not block the transmission of light in the wavelength region of 650 - 700 nm, where the main emission peak from this dye is.

Since the widely used software in SMLM, Picasso, is used in the workflow of this laboratory, I was encouraged to do calibration and localization with it as well. This would ensure the results and methods of this work to be more easily used later on.

### 3 Consideration of potential approaches

Three distinct approaches were first considered for the task: the use of a phase mask, a phase ramp or astigmatism-based methods. Each option was assessed based on their theoretical advantages, cost, complexity of physical implementation and complexity of post-imaging localization analysis.

#### 3.1 Phase mask

The phase mask approach has been considered the best approach theoretically, yielding a slightly better z-localization precision than an astigmatism-based method and also providing localization over a larger axial range ( $\sim 4\text{-}6\text{ }\mu\text{m}$ ). [17] [18] This approach needs a diffractive optical element with a complex pattern (phase mask) to be inserted into the Fourier plane of the microscope's light path. The characteristics of the phase mask would be dependent on the microscope and the emission wavelength of the fluorophores. With an older microscope system that lacked continued technical support and almost no commercial options to buy a phase mask, let alone a compatible one, the only way forward would have been to manufacture one. Manufacturing such a mask would have meant the use of a lithography machine to etch a pattern on a light-transmitting material (likely fused silica -  $\text{SiO}_2$ ), with smallest detail sizes of the pattern being on the order of a single micrometer. Such a service was not found in Tallinn. Closest options would have been Helsinki or Tartu. With no prior experience on phase mask design and manufacturing, it would have realistically taken several iterations to reach an acceptable result. The time requirements and cost of repeated travel, repeated use of a lithography machine service and multiple optical grade fused silica slabs would have been non-trivial. The phase mask would then have to be placed into a Fourier plane of the microscope. No Fourier plane location was accessible enough to have a new optical component added to it in a way that was stable and also easily removable. The Fourier plane would have to be created through what is known as a 4f system, requiring the addition of 2 lenses and extra space on the microscope's table. And finally, the post-imaging localization algorithm would have been more complex than with the simple elliptical Gaussian function fitting that an astigmatic-based approach would require. Considering all these factors, the phase mask approach was not favoured.

#### 3.2 Phase ramp

Of the three considered approaches, the phase ramp is the least documented one in scientific literature. Instead of a complex phase mask, it needs a thin glass slab with a straight edge and a linearly varying thickness. This wedge-shaped glass element would be inserted into the microscope's Fourier plane in a way that covers only half of the light path. This would in effect crudely imitate the phase shifting pattern of a double-helix phase mask, splitting the PSF into two rotating lobes. Microscopy slides have tolerances in their manufacturing, ensuring at least some uniformity, but there are still slight variances from one slide to another. One laboratory reported finding such a wedge-shaped glass among their bought microscopy slides that had enough of an angle between the two main faces to be used as a phase ramp in their microscope. [19] The low cost and potential ease of accessibility

of this method made it worth considering. As a simple initial test of this, several slides were cut into a smaller form and taped to the back of the objective (a Fourier plane), covering half of the aperture. While the shape of the PSF was indeed distorted, none of the tries yielded any result that was considered usable. Maybe a suitable slide was not among the ones experimented with. Maybe the microscope had an aberration that was incompatible with this method. Considering the phase ramp approach is a crude one that is not reported to yield a high z-localization precision nor axial range, and that the initial tests were not promising, this method was not explored further.

### **3.3 Astigmatism-based**

The astigmatism-based approach is the most popular in scientific literature. The z-localization precision is reported to be up to ~15-50 nm and the axial range is reported to be ~1-2  $\mu\text{m}$ . [20] [12] This is achieved by inducing astigmatism into the system with either a spatial light modulator, an electrically controlled deformable mirror or a simple cylindrical lens. Such an element would not be needed to be placed into the Fourier plane of the microscope, instead it could theoretically be placed anywhere in the light path after the objective. It is most commonly placed just before the camera. With a spatial light modulator or a deformable mirror the degree of astigmatism could be finely controlled via software. Such devices were, however, not already available in the laboratory, would have cost in the range of €4000-20000 and would have needed additional space on the microscope's table. With a cylindrical lens, the degree of astigmatism can be controlled by changing the distance of the lens from the camera. The complexity of post-imaging localization analysis would be the smallest with an astigmatism-based approach, with already several software tools developed to be capable of helping with this task. While an astigmatism-based approach is theoretically slightly inferior to a phase mask based approach, it was still chosen in consideration of all the other factors. The astigmatism inducing element was chosen to be a cylindrical lens.

## 4 Methodology

### 4.1 Cylindrical lens placement

The microscope had no prebuilt slot for this kind of modification. Most of the optical path resides in a large metal housing, which only allows the insertion of filters and mirrors. These insertion slots were already in use, needed in dSTORM imaging. The only possible accessible location for adding an extra element was the space between the relay lens and the camera. This space had a length of about 13 cm. Moving the camera closer to or further from the relay lens would have changed the physical size that each pixel represented on the image. At the aforementioned distance, a pixel represented 70 nm of physical size when used with a 100x objective. This pixel-to-size ratio is seen as a good ratio in dSTORM imaging and should ideally be maintained. Adding additional lenses would have allowed to lengthen this distance, but every optical element added into the optical path will absorb or deflect some of the light. With fluorophores already emitting light at low intensities and maximizing photon count improving localization in dSTORM imaging, adding more optical elements than necessary is to be avoided. The space of 13 cm would hopefully be enough to work with.

The degree of astigmatism here would depend on the focal length of the cylindrical lens and the distance of its placement from the camera. A shorter focal length cylindrical lens would effect a stronger degree of astigmatism on the image. A longer distance between the lens and the camera would also result in stronger astigmatism. The existing scientific literature did not have a guide on how to choose these parameters for an optimal degree of astigmatism when using a cylindrical lens. The optimal position will vary between microscopes if the lenses used (objective, tube lens, relay lens...) in the light path are different. Two papers mentioned using a  $f = 1000$  mm focal length cylindrical lens. [10] [21] This then became the practical starting point to be also tested in this work. The first cylindrical lens bought was LJ1516RM-A by Thorlabs (Figure 7). It is a 1000 mm focal length plano-convex cylindrical lens, made out of borosilicate-crown glass material - N-BK7. This material has an over 90% transmission rate in the 650-700 nm wavelength range we are working with. It also features an antireflection coating that covers this range, reducing the chance of incoming light being reflected off it. Diameter of the lens (glass + housing) is 1 inch, which is a standard size often used with optical elements, allowing compatibility with various mounts. Initial testing of the lens at various distances from the camera within the given 13 cm space resulted in degrees of astigmatism that were somewhat underwhelming compared to images seen in scientific papers. Two similar lenses were then additionally bought that featured smaller focal lengths: LJ1144RM-A ( $f = 500$  mm) and LJ1267RM-A ( $f = 250$  mm). Trying these individually at various distances from the camera resulted in a degree of astigmatism seen in scientific literature and higher.



**Figure 7:** Plano-convex cylindrical lens, LJ1516RM-A, by Thorlabs. Focal length of  $f = 1000$  mm, diameter of 1 inch and made out of light transmissible borosilicate-crown glass material - N-BK7.

For easy removal from and reapplication of the lenses to the light path of the microscope, they were mounted into a filter wheel (Figure 8), capable of quickly switching between the three lenses or no lens at all. With the housing of the filter wheel taking up a little bit of extra space, the range where the lenses were able to be positioned was shortened to under 10 cm. To investigate the different degrees of astigmatism possible with these three lenses in this given space, imagings were done at 5 locations within this range with all three lenses. Starting out at a 3.5 cm distance between the camera housing and the filter wheel, increasing the distance with 1.5 cm at each step, up to the last distance of 9.5 cm. The distance from the exterior housing of the filter wheel to the center of the cylindrical lens was 0.8 cm. The camera chip was positioned 1.2 cm inward from the outer housing of the camera. By adding these offsets to the measured distances between the camera housing and the filter wheel, we obtain the five used distances between the cylindrical lens and the camera chip: 5.5, 7.0, 8.5, 10.0, and 11.5 cm.



**Figure 8:** Filter wheel connected to the camera and microscope housing with lens tubes.

Various length lens tubes, found among the equipment stockpile of the laboratory, were used to fill in the spaces between 1) the camera chip and the filter wheel and also 2) the filter wheel and the relay lens. These lens tubes blocked unwanted light from reaching the camera chip and held the testing setup stable. Each time this setup was rebuilt to change the location of the filter wheel, the pixel-to-size ratio of the camera was recalibrated with the help of an objective micrometer to ensure 70 nm per pixel.

## 4.2 Imaging z-stacks

The usage of Alexa Fluor 647 fluorophores in these imagings was not possible, as they are not meant for long duration experiments and would have exhibited photobleaching, becoming progressively dimmer within minutes of being excited with a laser. To ensure a stable signal throughout testing, some other sub-diffraction sized fluorescent objects with a similar emission wavelength to Alexa Fluor 647 were needed. Both fluorescent microspheres and quantum dots were tested. CdTe quantum dots with a claimed emission wavelength peak of  $670\pm 5$  nm and diameter of  $\sim 4.0$  nm were tried, but exhibited a very dim signal and stochastic blinking (in this case unwanted). The microspheres finally used were the deep red variant from PS-Speck Microscope Point Source Kit by ThermoFischer with a claimed emission wavelength peak of 660 nm and a diameter of  $175\pm 5$  nm. The microspheres resulted in a stable signal and were thus chosen for further usage.

The microspheres were transferred to a slide in a water solution, which was then left to dry out. This resulted in the microspheres to be fixed onto the slide, all at the same plane. Immersion oil with a refractive index of  $n = 1.518$  was added on top before sealing with a coverslip. A 100x objective from Zeiss (NA= 1.45) was used with the same immersion oil also added between the objective and the slide. The microspheres were excited with the 640 nm laser. For imaging, regions on the slide were located where there were several microspheres visible, but where they were still sufficiently spread apart to not have their PSFs overlap each other.

To capture the 3D astigmatic PSFs of the microspheres, several images would have to be taken of them at different focal depths. A series of such images is called a z-stack. The microscope was capable of making such z-stacks with a 10 nm spacing between focal planes. Previous experiments in scientific literature have claimed a maximum usable axial range of  $\sim 1-2$   $\mu\text{m}$  for astigmatic PSFs. To be absolutely certain of capturing all of that range, I imaged PSFs of the microspheres over an axial range of 6  $\mu\text{m}$ . In order to get clear images of the PSFs, the z-stacks were first done with laser power of 10 mW. These z-stacks were later used to best characterize the exact shapes of the PSFs at each degree of astigmatism. Since in real dSTORM imaging, the SNR of the fluorophores is much lower, there was a need to also simulate such conditions. To induce lower SNR during testing, the laser intensity was gradually lowered and at each step a new z-stack was taken. The different laser power values used were (in mW): 10; 8; 6; 4; 2; 1; 0.8 and 0.6. At laser power below 0.6 the microspheres were often not being excited anymore and no further z-stacks with lower laser intensities were attempted. It is important to note here that the light intensity reaching the microspheres was significantly lower than what was set in the software interface and that this will vary between setups. Some of the light intensity got lost with mirrors directing the laser on to the sample. Also, TIRF illumination mode was

used during the experiment to imitate conditions used with real dSTORM imaging, further reducing the amount of energy reaching the sample. An exposure time of 50ms was used at each frame.

To summarize, there were z-stacks taken at 8 different laser intensities, at 5 different locations for the cylindrical lens and at each location 3 different lenses were separately used. This results in a total number of 120 z-stack files, each 1.2 GB in size. With a z-stack spanning over a 6  $\mu\text{m}$  axial range with 10 nm steps, it contains 600 images. This brings us to a total of 72000 images at 144 GB. These final imagings were done over the course of 3 days.

### 4.3 Post-imaging data processing

To evaluate which laser intensity resulted in z-stacks with a SNR nearest to a real dSTORM imaging, one option is to compare their peak SNRs. Since photon counts at each pixel follow Poisson statistics this can be done via this practical estimator [22]:

$$\text{SNR} = \max_v \sqrt{\frac{1}{9} \sum_{\delta \in \{-1,0,1\}^2} i_{v+\delta}} \quad (13)$$

where  $i$  is the intensity at any given pixel  $v$ .

This process involves using a 3x3 kernel at each pixel to average its values with the neighbouring pixel values, taking the square root of it and then finding the maximum resulting value among all pixels. Having access to some previously done dSTORM imagings and also randomly sampling some frames from the acquired microsphere z-stacks, peak SNR was calculated on them using this estimator. The results indicated that the z-stacks made with 1 mW laser power had the most similar SNR values to dSTORM imaging conditions.

Another option is to compare photon counts yielded per PSF. At the 1 mW level, the photon count per PSF was 300. This is significantly lower than in real dSTORM imaging, where 1000 - 2000 photons per PSF is average. At 2 mW, the average photon count was 800, which is still lower than in real conditions. Considering the SNR and photon counts, only the z-stacks done with 10 mW and 2 mW laser intensity were relevant going forward. The 10 mW ones were to be used for calibration. The 2 mW ones were to be used for estimation of localization precision in a low SNR and photon count situation that approximated real dSTORM imaging conditions.

The Picasso software, which was encouraged to be used in this work for localization, uses a 2D elliptical Gaussian function (see Equation 12) fitting that assumes the axes of the ellipse are already aligned with those of the image. In effect, this means that either the cylindrical lens must be perfectly rotated before imaging to match the axes of the camera chip or the images must be rotated manually before analysis with Picasso. Since the process in this work included the dismantling and rebuilding of the setup multiple times to change the location of the cylindrical lens, it was difficult to keep the lens axes always perfectly aligned with the camera's. The rotation was thus applied (Figure 9) to each relevant z-stack during post-imaging processing with the help of ThunderSTORM plugin on ImageJ

software. ThunderSTORM features a rotated elliptical Gaussian PSF function fitting model, which gives the user the angle of the PSF ellipses compared to the image's. This elliptical Gaussian PSF fitting logic follows the model described in the supplementary notes of Ovesný et al. (2014) [23]:

$$PSF(x, y | \theta, \phi) = \frac{\theta_N}{2\pi\theta_{\sigma_1}\theta_{\sigma_2}} \exp\left(-\left[\frac{x'^2}{2\theta_{\sigma_1}^2} + \frac{y'^2}{2\theta_{\sigma_2}^2}\right]\right) + \theta_b \quad (14)$$

where  $PSF$  is the expected photon count at pixel position  $(x, y)$ ,  $\theta$  represents a vector of fitting parameters and  $(x', y')$  represents rotated coordinates:

$$\begin{aligned} x' &= (x - \theta_x) \cos \phi - (y - \theta_y) \sin \phi \\ y' &= (x - \theta_x) \sin \phi + (y - \theta_y) \cos \phi \end{aligned}$$

The angle  $\phi$  can be then calculated by:

$$\phi = \frac{1}{4} \text{atan2}\left(\frac{1}{n} \sum_{i=1}^n \sin \phi_i, \frac{1}{n} \sum_{i=1}^n \cos \phi_i\right) \quad (15)$$

After acquiring this angle, the z-stack was rotated to a manner suitable for analysis with Picasso.

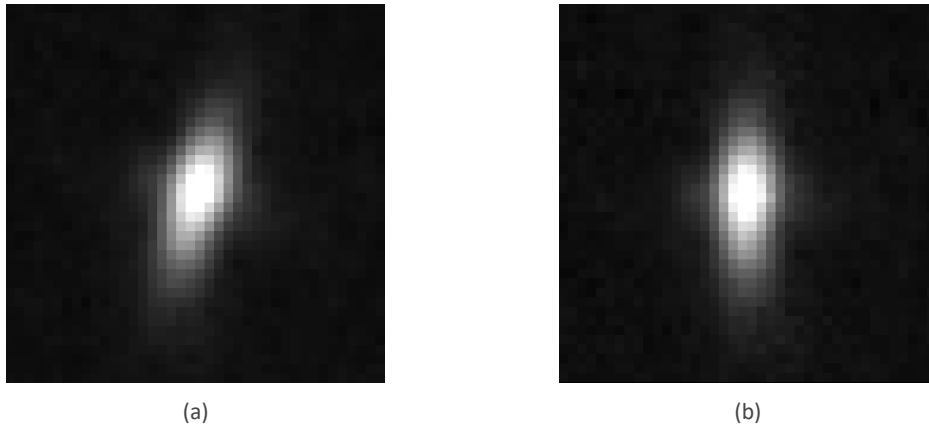


**Figure 9:** An astigmatic PSF from a frame in one of the z-stacks, before (a) and after (b) rotating to align its axes with the image's.

After this step, the z-stacks were visually examined for any PSFs not suitable for further analysis. Even though regions of the sample were imaged that had a sparse population of microspheres, at a high degree of astigmatism some PSFs stretched large enough to still overlap each other. Also, there were some instances where dust on the camera or on the lenses was present and distorted some singular PSFs. In both of these cases, the affected regions of the z-stacks were cropped out. For calibration, clear PSF shapes are desired.

To do 3D localizations with Picasso one first has to calibrate it by characterizing how the PSF's ellipticity with the current optical setup changes in response to variations in focal depth. Picasso can help do that as well. Given a z-stack, it will detect the approximate locations of PSFs in each frame

and fit those with the elliptical Gaussian function. In each frame it averages the standard deviation of the two axes of each fitted PSF. Then the mean standard deviations throughout the z-stack are fitted with an even-order polynomial function:

$$s_x(z) = c_x[0] \cdot z^0 + c_x[1] \cdot z^1 + \dots + c_x[6] \cdot z^6$$

$$s_y(z) = c_y[0] \cdot z^0 + c_y[1] \cdot z^1 + \dots + c_y[6] \cdot z^6$$

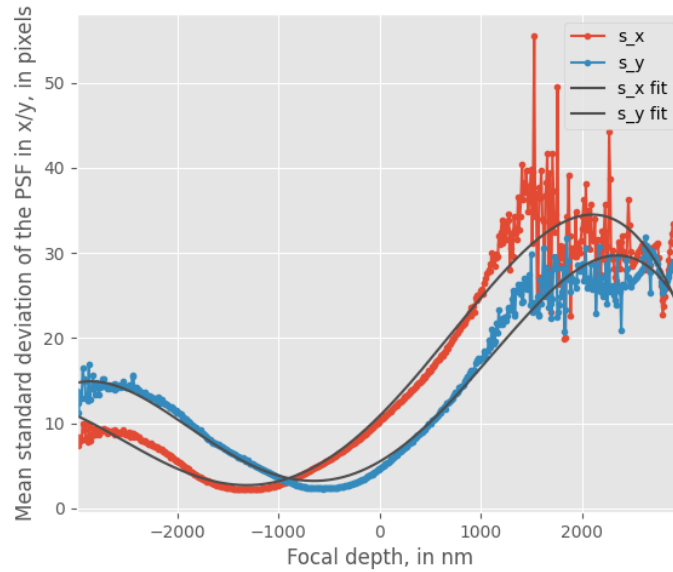


**Figure 10:** Mean standard deviation of the PSF height and width dependent on the focal position of the microscope. Black lines represent the polynomial fits. Focal length  $f = 1000$  mm cylindrical lens used, situated 11.5 cm from camera chip. Axial range of  $6 \mu\text{m}$  is presented. Picasso

At focal depths far from the microspheres, the PSFs became more difficult to fit, as seen on Figure 10. As previously mentioned, scientific literature has reported a maximum axial range of  $\sim 1\text{-}2 \mu\text{m}$  to be usable with 3D localization via astigmatism. Considering this and also the observation that PSFs from far out of focus frames negatively contribute to the accurate fitting of the polynomial functions, the axial range of the z-stacks were deemed to be shortened from  $6 \mu\text{m}$  down to  $2.6 \mu\text{m}$ . ImageJ has simple tools to cut frames from z-stacks. The new, shortened z-stacks were centered with the frame where the microspheres were most in focus. A padding of  $\pm 1.3 \mu\text{m}$  was left on either side, resulting in 261 frames per z-stack. The center frame was ascertained by the intersection of the blue and red lines on Figure 10, where the mean height and width of the PSFs matched. Now with the new, shorter z-stacks, more accurately fitted calibration curves were possible to be made (Figure 11). These calibration curves were then used for z-position localization on the lower photon count 2 mW z-stacks with respective degree of astigmatism.

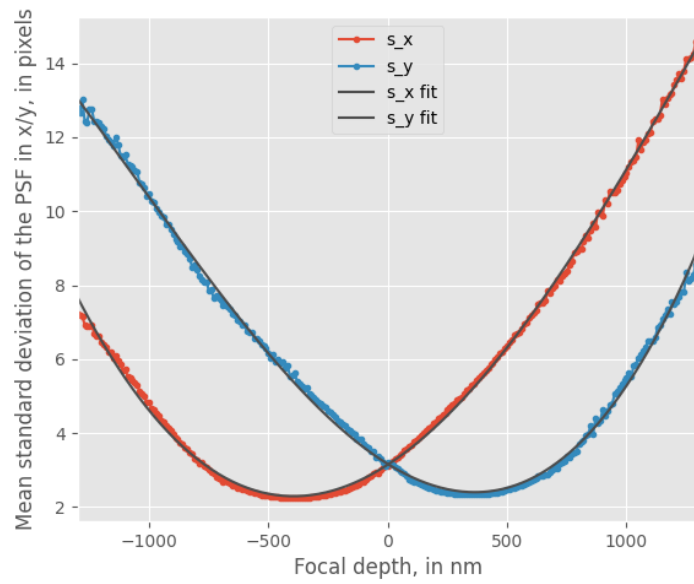


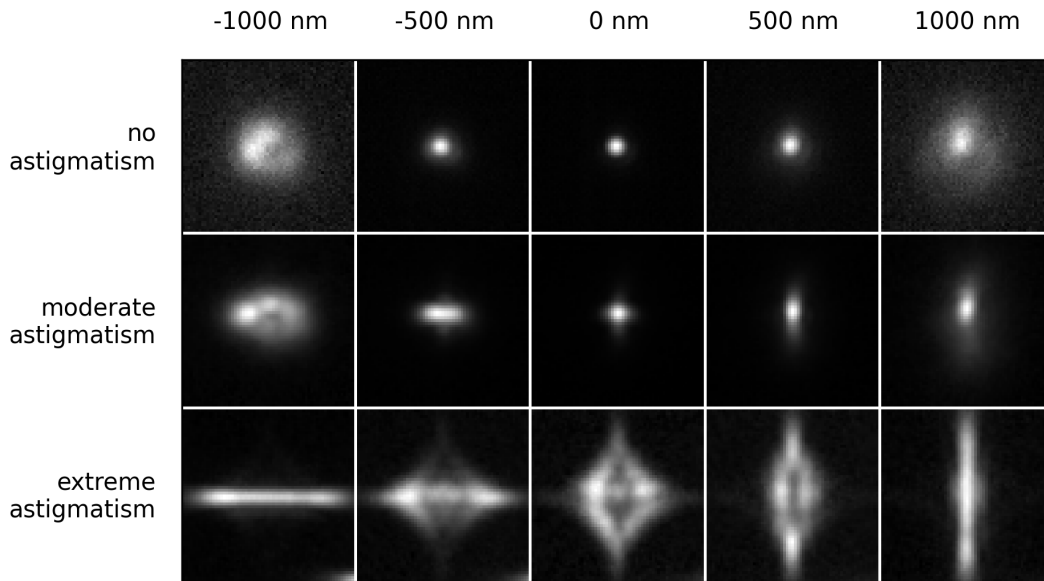
**Figure 11:** Mean standard deviation of the PSF height and width dependent on the focal position of the microscope. Black lines represent the polynomial fits. Focal length  $f = 1000$  mm cylindrical lens used, situated 11.5 cm from camera chip. Axial range of  $2.6 \mu\text{m}$  is presented. Picasso

Throughout the post-imaging data processing, ImageJ macro capabilities and custom Python scripts were invaluable to manipulate the vast numbers of frames over the dozens of z-stacks.

## 5 Results

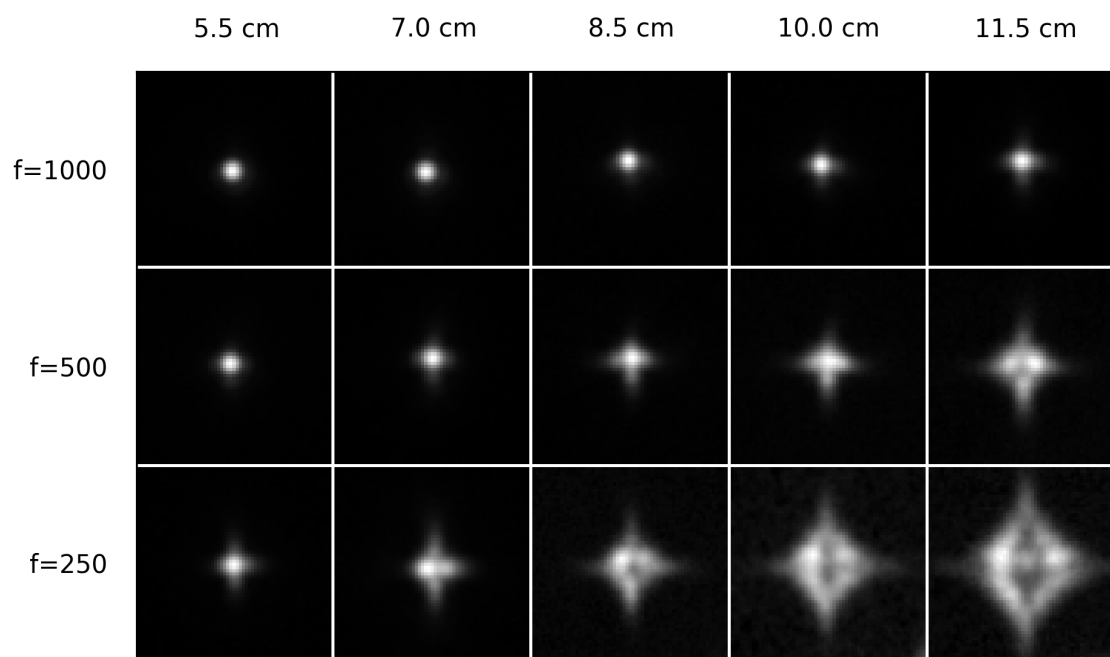
### 5.1 Point spread function shapes

All the PSF shapes in this subchapter are shown from z-stacks where the highest laser intensity setting (10 mW) was used. This is done to first clearly understand how the PSF shape morphs under various degrees of astigmatism and defocus.



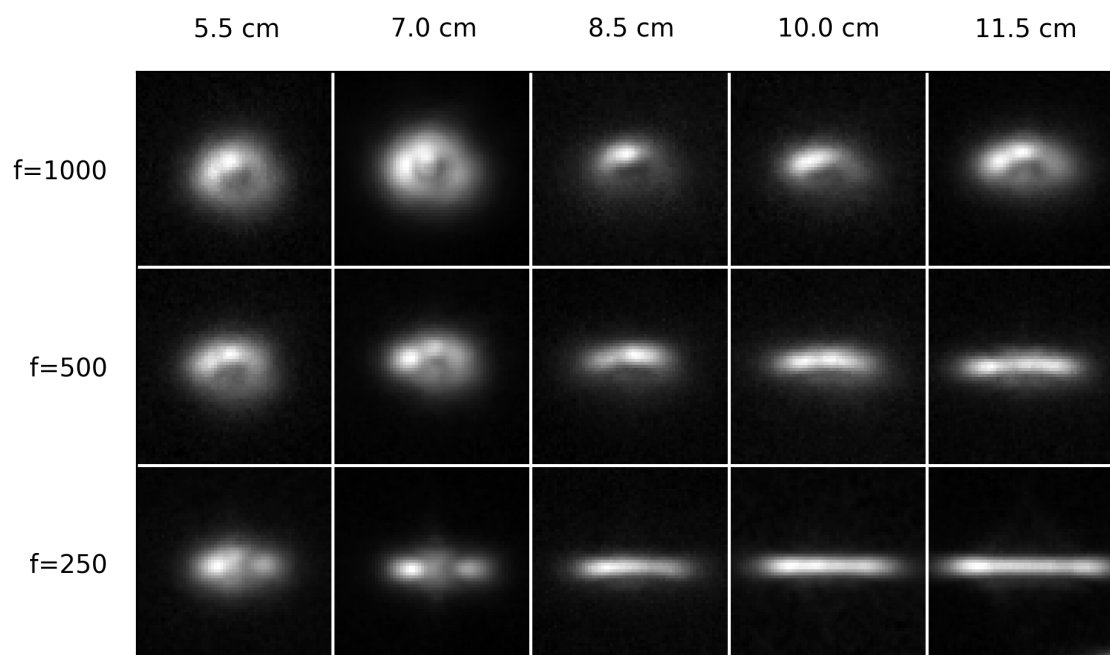
**Figure 12:** PSF shapes with various degrees of astigmatism and various defocus from the center of the microspheres. Upper row showing the PSFs with no cylindrical lens added. Second row showing the PSFs with the  $f=500$  mm cylindrical lens at distance 5.5 cm. Lower row showing the PSFs with the  $f=1000$  mm cylindrical lens at distance 11.5 cm. 10 mW laser power used. Each picture was independently contrast-enhanced via local min–max normalization.

From Figure 12 we can see astigmatism was indeed applied by adding a cylindrical lens to the light path and that different degrees of astigmatism were achieved. These cases we can compare with the upper row of the figure, where no astigmatism was present. Varying the location of the focal plane clearly changes the elongation axis and magnitude of the PSFs. At the focal plane centered on the microspheres, with a high degree of astigmatism, the PSF takes on a more complex shape that does not visually resemble an elliptical Gaussian.



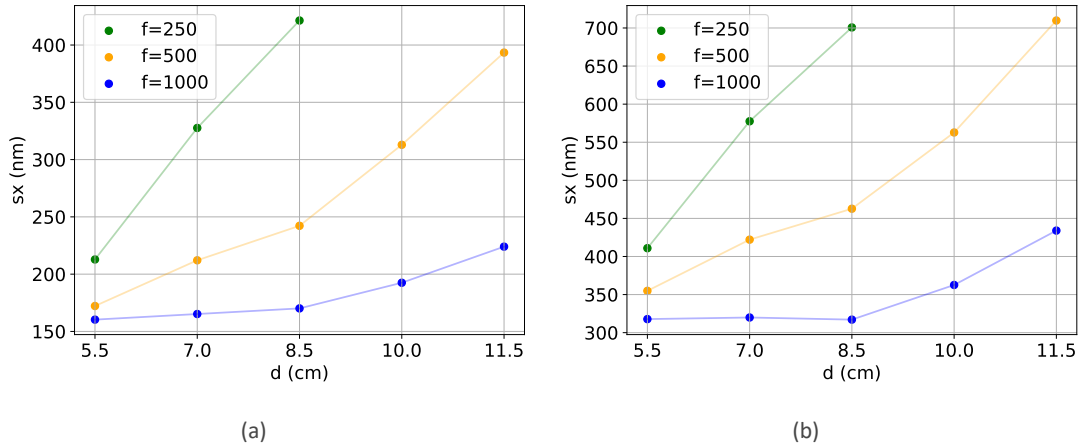
**Figure 13:** PSF shapes shown at the center focal plane (0 nm defocus) with varying degrees of astigmatism. Three cylindrical lenses with varying focal lengths  $f$  used (given in mm). Five different distances between the EMCCD camera chip and the center of the lens. All images are at the same scale of 63x63 pixels (4.41x4.41  $\mu\text{m}$ ). 10 mW laser power used. Each picture was independently contrast-enhanced via local min-max normalization.

Figure 13 shows the varying degrees of astigmatism achieved with the 15 different configurations (3 lenses, 5 locations). All of these PSFs are captured at the center frame of the z-stacks, where the microspheres are directly at the focal plane. It is evident that with higher degrees of astigmatism the PSFs occupy a relatively very large space on the image. Looking at figure 3 we see how close together blinking events in dSTORM imagings can be. Limiting the PSF size is crucial in order to not have them overlap each other on crowded frames. Thus, the higher degrees of astigmatism here with a cylindrical lens of focal length  $f = 250$  mm can be immediately deemed as not favoured to be used.



**Figure 14:** PSF shapes shown at a focal plane away from the microspheres (-1000 nm defocus) with varying degrees of astigmatism. Three cylindrical lenses with varying focal lengths  $f$  used (given in mm). Five different distances between the EMCCD camera chip and the center of the lens. All images are at the same scale of 63x63 pixels (4.41x4.41  $\mu\text{m}$ ). 10 mW laser power used. Each picture was independently contrast-enhanced via local min-max normalization.

Figure 14 shows the varying degrees of astigmatism achieved with the 15 different configurations (3 lenses, 5 locations) at -1000 nm defocus from the microspheres. We would see similar images with a +1000 nm defocus, only the elongation would be along a perpendicular axis to this case. The space occupied by the PSF on the image at this defocus level does not seem to be drastically increasing with astigmatism as we saw in Figure 13. A moderate degree of astigmatism might even reduce the PSF size. We can also see from these images that there is some unwanted aberration present in the system, with some of the PSFs having a brighter upper part than the lower part. The origin of this aberration could have existed in the microscope already before this experiment. While manufacturers do add multiple corrective lenses inside the objective to reduce aberration, it can never be perfectly eliminated. This aberration could also stem from slight angle mismatches between the relay lens, the cylindrical lens and the camera chip. Perfect alignment during dismantling of external part of the system (seen on Figure 8) and rebuilding it multiple times was difficult to achieve.



**Figure 15:** Evolution of PSF widths at different degrees of astigmatism shown. The effect of the three different focal length  $f$  (given in mm) lenses shown in different colors. X-axis showing the different positions of the lenses, y-axis showing the standard deviation of the width of the PSFs. (a) No defocus is present. PSF width is measured at the focal plane of the microspheres. (b) PSF widths are measured at a defocus level of -500 nm.

On Figure 15 (a) we can see the standard deviations of the widths of the elliptical Gaussian functions (see Equation 12 that the PSFs were fitted with at various degrees of astigmatism at 0 nm defocus level. On image (b) the defocus is at -500 nm. The widths seem to be increasing relatively linearly with increased astigmatism. When using a smaller focal length cylindrical lens (stronger astigmatism) the degree of astigmatism increases faster with increasing the distance. Some configurations of the lens and distance used result in a similar degree of astigmatism, as is also expected. For example, setting the  $f=500$  mm focal length cylindrical lens at a distance of 5.5 cm from the camera results in a relatively similar PSF widths to the configuration of setting the  $f=1000$  mm focal length lens at 10 cm from the camera. Interestingly here, even though the PSF shapes with higher degrees of astigmatism became visually very complex at 0 nm defocus level (as seen from Figure 13), the elliptical Gaussian function was still able to fit them accurately enough to keep the linear trend.

## 5.2 Elliptical Gaussian function fitting at lowered laser light

The polynomial calibration curves for each configuration (3 lenses, 5 locations) were done with a strong laser light intensity (10 mW). Those calibration curves were then used to judge the z-location of PSFs at a lower laser light intensity (2 mW) with photon counts per PSF that are slightly below of that yielded in real dSTORM imagings. An example of this is depicted at Figure 16.

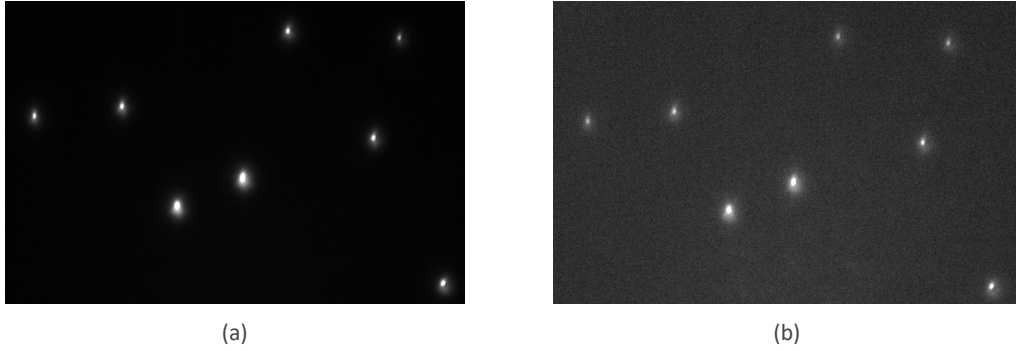
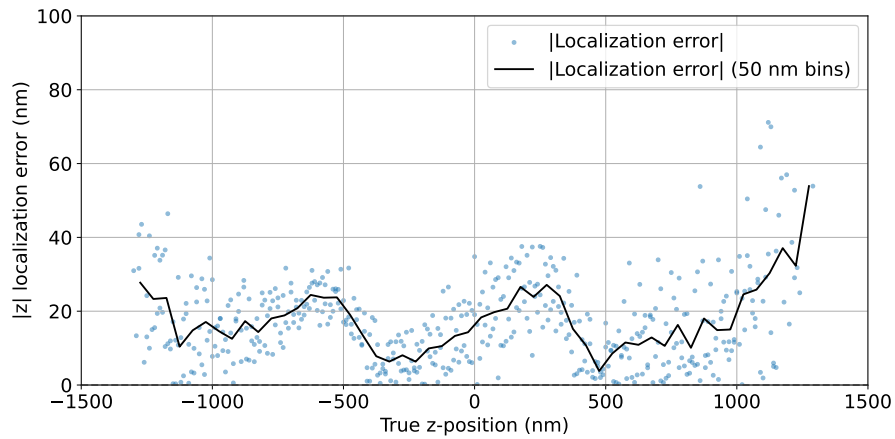
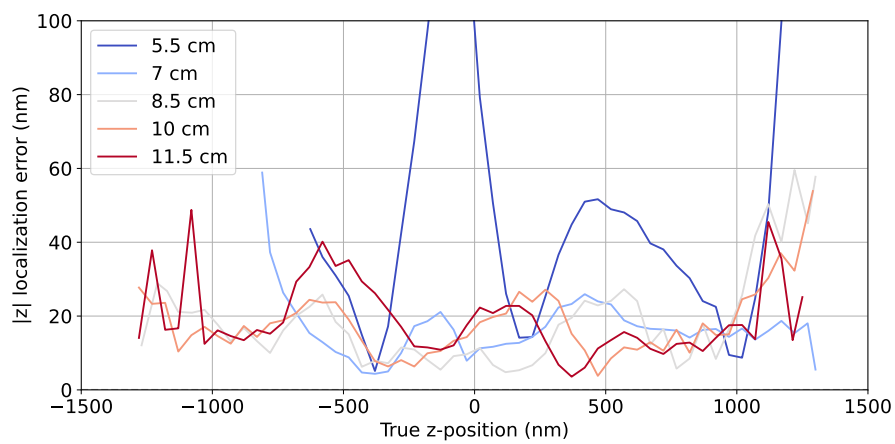


**Figure 16:** Moderately astigmatic PSFs at (a) 10 mW and (b) 2 mW laser light intensities. Defocus level is 1000 nm. Focal length of  $f=1000$  mm cylindrical lens is placed at 7 cm from the camera. Both pictures were independently contrast-enhanced via local min–max normalization.

Using the previously acquired calibration curves we can estimate the  $z$ -positions of microspheres at different frames on the 2 mW  $z$ -stacks. The true positions we know from the frame number, as the microspheres are in focus on the center frame and each consecutive frame away from the center is a 10 nm focus shift step. Comparing the estimated  $z$ -position to the known  $z$ -position we can see how much the estimation is off. All of the following data is at a focus range of -1300 nm to +1300 nm, as defocus levels higher than  $1\ \mu\text{m}$  quickly leads to a spread out PSF that is not possible to localize accurately.



(a)



(b)

**Figure 17:** Mean  $|z|$  localization error shown as a function of defocus level away from the center of the microspheres. Figure (a) exemplifying the individual localization data in just one distance (10 cm) and Figure (b) showing all five distances.  $f = 1000$  mm focal length cylindrical lens placed at 5 different distances. Data binned at 50 nm intervals.

On Figure 17 the mean  $|z|$  localization error is shown at different defocus levels with the  $f = 1000$  mm lens at different lengths from the camera. When the lens is closest to the camera (5.5 cm), it does not result in large enough distortion to the PSF that different  $z$ -positions are well distinguishable. This especially at the center focus, where localization error spikes and at higher defocus levels, where localization completely breaks down and no data points were acquired. With the next position (7 cm) the center localization error already diminishes, but at large negative defocus levels the yet again breaks down and no data is shown. From that distance on, in rest of the cases, the mean error stays relatively stable throughout the  $-1 \mu\text{m}$  to  $+1 \mu\text{m}$  range and starts being less reliable after that.

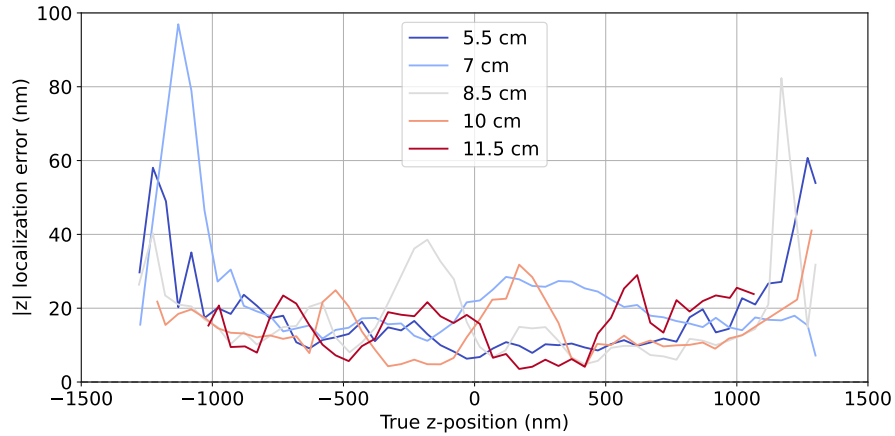


**Figure 18:** Mean  $|z|$  localization error shown as a function of defocus level away from the center of the microspheres.  $f= 500$  mm focal length cylindrical lens placed at 5 different distances. Data binned at 50 nm intervals.

Figure 18 depicts the mean  $|z|$  localization error when using the  $f= 500$  mm lens. The error is again relatively low and stable in the  $-1 \mu\text{m}$  to  $+ 1 \mu\text{m}$  range and stays this way throughout all 5 distances.

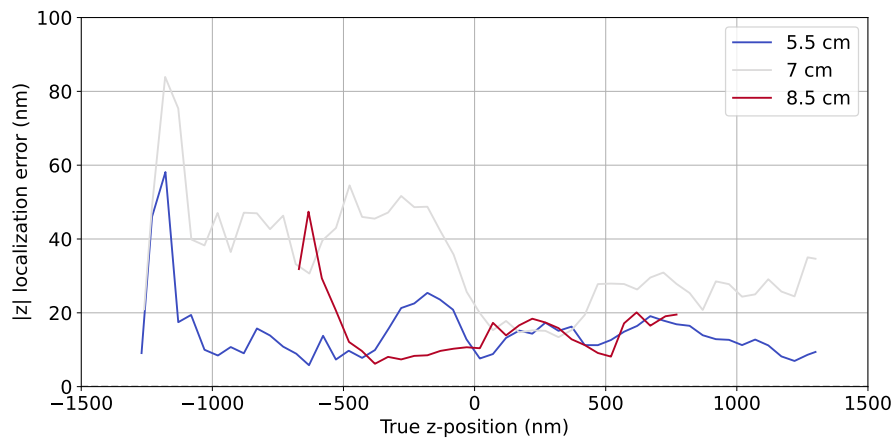


**Figure 19:** Mean  $|z|$  localization error shown as a function of defocus level away from the center of the microspheres.  $f= 250$  mm focal length cylindrical lens placed at 5 different distances. Data binned at 50 nm intervals.

Figure 19 depicts the mean  $|z|$  localization error when using the  $f= 250$  mm lens. The error is good with the shortest distance used (5.5 cm), but increases with the second distance (7 cm). With the third distance (8.5 cm) the PSF is too spread out and localization starts to fail outside of the  $-0.5 \mu\text{m}$  to  $+ 0.5 \mu\text{m}$ . At the two remaining distances (10 cm and 11.5 cm) Picasso was not able to even generate calibration curves, as again, the PSF shapes became too spread out and detection of the whole PSF as a single entity became unreliable.

Table 1 shows the aggregated data from these results.

Distance	Mean $ z $ error in $[-500, +500]$ nm			Mean $ z $ error in $[-1000, +1000]$ nm		
	f = 1000 nm	f = 500 nm	f = 250 nm	f = 1000 nm	f = 500 nm	f = 250 nm
5.5 cm	54.2	10.8	15.1	46.3	12.8	14.1
7 cm	14.5	20.8	30.3	16.3	19.5	32.2
8.5 cm	11.3	16.8	–	13.9	14.4	–
10 cm	14.9	13.3	–	15.5	12.9	–
11.5 cm	17.1	11.4	–	17.6	14.5	–

**Table 1:** Comparison of mean  $|z|$  localization errors at different focal lengths and depth ranges.

## 6 Discussion

The work in this thesis involved using astigmatism to enhance an existing microscope with 3D SMLM imaging capability. Cylindrical lenses with different focal lengths were tested at various distances from the microscope's camera and such combinations were found where the mean  $|z|$  localization accuracy of  $\sim 15$  nm were achieved over a range of  $2\ \mu\text{m}$ .

With most of the tested lens + distance configurations the z-localization mean absolute error was similar to that found in scientific literature at focus levels near the microspheres. At greater than 500 nm defocus, the localization error is often reported to start increasing. This was not really the case in this work, where the same mean localization error of  $\sim 15$  nm did not increase much after 500 nm defocus to near 1000 nm. It only started to increase significantly at or after 1000 nm defocus level. I suspect that, even though the photon count per PSF at 2 mW laser intensities was slightly even below what one would get at a real dSTORM imaging, the SNR was still too good. A lot of the noise in dSTORM imaging would come from background fluorescence, which was absent in this case. The primary source of noise in this experiment was intended to come from the camera. EMCCD cameras are exceptionally good at imaging in low light conditions though and add very little noise to the image. Maybe the high degree of z localization precision came because of this. If that is true, then a more accurate imitation of real dSTORM conditions would have been achieved by adding extra noise onto the 2 mW z-stacks. With more noise, the microsphere z-locations at central focus would still have been accurately determined, but out of focus PSFs would have blended into the noise more and been harder to localize. Adding noise post-imaging would have meant one has to first characterize the typical levels of Poisson and Gaussian noise present in dSTORM imaging. This is difficult as these can vary between experiments.

It can still be concluded from this work that the weakest astigmatism configuration ( $f= 1000$  mm lens at 5.5 cm distance) is definitely not a good choice. The distortion was not big enough to be distinguishable, especially at the central focus frames. The localization with the second weakest configuration ( $f= 1000$  mm lens at 7 cm) was better in the center frames, but also failed after negative  $\sim 800$  nm focus. Configurations with stronger astigmatism after that yielded a good z-localization throughout  $-1000$  to  $+1000$  nm. Since larger PSFs would start to occupy more area on the image and inevitably also overlap with other PSFs nearby, it is better to avoid these if possible. Larger PSFs would also lead to worse x- and y- localizations, as they would blend in to noise easier. Therefore the best configuration options would be any one just after the first two weakest configurations. The configuration of  $f= 1000$  mm lens at 8.5 cm would be the best choice, with  $f= 1000$  mm lens at 10 cm and  $f= 500$  mm lens at 5.5 cm also being good choices.

## **7 Acknowledgments**

I would like to express my gratitude to my supervisor, Martin Laasmaa, for his time and guidance in helping me complete this work, and for consistently providing prompt answers to my questions. I would also like to acknowledge Irina Česnokova for her patience in training me on the laboratory equipment.

This work was supported by the Estonian Research Council grant (PSG 832).

## Abstract

Advancements in super-resolution microscopy are allowing the study of biological systems at an ever finer detail. Among the various methods aiming to image at sub-diffraction limit resolution, one of the leading techniques is dSTORM, belonging to the subgroup of a technique called single-molecule localization microscopy (SMLM). While initially, it could only be used for 2D imaging, there have been developments that allow extracting molecules' position along the z-axis from 2D images by modifying an optical system's point spread function (PSF), thus pushing the technique into the realm of 3D imaging.

This thesis goes through the process of implementing one of such modifications, inducing z-axis-dependent changes in the PSF of fluorophores by leveraging astigmatism via a cylindrical lens. Three cylindrical lenses of different focal lengths were tested at five locations in the microscope's light path. Fluorescent microspheres were excited with a laser, and their respective PSF shapes were recorded at various focal depths over a range of [-1300, +1300] nm. Using this data as calibration, the microspheres were again imaged over a range of focal depths at lower laser intensity, imitating low photon yield dSTORM conditions, the z-localization accuracy was obtained for the various combinations of lens and location. From these results, the optimal configuration for the given microscope was determined, and its z-localization accuracy was characterized.

In summary, this work enhanced the microscope's light path to allow 3D dSTORM imaging. In addition, by documenting the steps needed to determine a compatible configuration of a cylindrical lens and its location in the microscope's light path, explaining the problems encountered in the process, and showing the tools used to carry out this method, this thesis can also serve as a guide for others aiming to upgrade their dSTORM setups.

## Annotatsioon

Arengud superresolutsiooni mikroskoopias võimaldavad bioloogiliste süsteemide uurimist üha suurema detailsusega. Üks juhtivaid ja laialt kasutatavaid superresolutsiooni meetodeid, mis suudab objekte kujutada alla difraktsioonipiiri ulatuva eraldusvõimega, on dSTORM, mis kuulub tehnikate alamrühma nimega üksikmolekuli lokaliseerimismikroskoopia (SMLM). Kui algselt oli võimalik kasutada seda tehnikat vaid 2D-kujutamiseks, siis arengud optiliste süsteemide punktihajuvusfunktsiooni (PSF) muutmises on võimaldanud molekulide asukoha määramist ka z-teljel 2D-kujutiste põhjal, tõstes tehnika 3D-kujutamise valdkonda.

Käesolevas lõputöös käsitletakse ühe sellise modifikatsiooni teostamist, kus fluorofooride PSF-e muudetakse z-teljest sõltuvalt, kasutades astigmatismi tekitamiseks silindrilist läätsed. Katsetati kolme erineva fookuskaugusega silindrilist läätsed viies erinevas asukohas mikroskoobi valgustekonnal. Fluorestseeruvad mikrosfäärid ergastati laseriga ja nende vastavad PSF-kujud salvestati erinevatel fookussügavustel vahemikus [-1300, +1300] nm. Selle andmestiku põhjal kalibreeriti süsteem ning mikrosfäärid pildistati uuesti madalama laseri intensiivsusega, imiteerides madala footonisaagisega dSTORM-tingimusi. Saadud andmete põhjal määrati z-lokaliseerimise täpsus erinevate läätsede ja nende asukoha kombinatsioonide korral. Tulemuste põhjal leiti antud mikroskoobi jaoks optimaalne konfiguratsioon ning määratleti selle z-lokaliseerimise täpsus.

Kokkuvõttes muudeti käesolevas töös mikroskoobi valgustekonna konfiguratsiooni, võimaldamaks 3D-kujutamist dSTORM tehnikat kasutades. Lisaks, kuna töös on dokumenteeritud vajalikud sammud sobiva silindrilise läätsed ja selle asukoha määramiseks mikroskoobi valgustekonnal, selgitades protsessis ette tulnud probleeme ning kasutatud tööriistu, on antud töö ka juhendiks teistele, kes soovivad oma dSTORM kuvamist viia uuele tasemele.

## References

- [1] Bo Huang, Hazen Babcock, and Xiaowei Zhuang. “Breaking the Diffraction Barrier: Super-Resolution Imaging of Cells”. In: *Cell* 143.7 (Dec. 2010), pp. 1047–1058. DOI: 10.1016/j.cell.2010.12.002.
- [2] E. Abbe. “Beiträge zur Theorie des Mikroskops und der mikroskopischen Wahrnehmung”. In: *Archiv für Mikroskopische Anatomie* 9.1 (Dec. 1873), pp. 413–468. DOI: 10.1007/BF02956173.
- [3] Max Born, Emil Wolf, and A. B. Bhatia. *Principles of optics: electromagnetic theory of propagation, interference, and diffraction of light*. en. Seventh (expanded) anniversary edition, 60th anniversary edition. Cambridge: Cambridge University Press, 2019, pp. 439–443.
- [4] M. G. Gustafsson. “Surpassing the lateral resolution limit by a factor of two using structured illumination microscopy”. eng. In: *Journal of Microscopy* 198.Pt 2 (May 2000), pp. 82–87. DOI: 10.1046/j.1365-2818.2000.00710.x.
- [5] S. W. Hell and J. Wichmann. “Breaking the diffraction resolution limit by stimulated emission: stimulated-emission-depletion fluorescence microscopy”. eng. In: *Optics Letters* 19.11 (June 1994), pp. 780–782. DOI: 10.1364/ol.19.000780.
- [6] W. Mark Bates et al. “Multicolor Super-resolution Imaging with Photo-switchable Fluorescent Probes”. In: *Science (New York, N.Y.)* 317.5845 (Sept. 2007), pp. 1749–1753. DOI: 10.1126/science.1146598.
- [7] Honglin Li and Joshua C. Vaughan. “Switchable Fluorophores for Single-Molecule Localization Microscopy”. In: *Chemical reviews* 118.18 (Sept. 2018), pp. 9412–9454. DOI: 10.1021/acs.chemrev.7b00767.
- [8] NIKON. *N-STORM | The principle of Stochastic Optical Reconstruction Microscopy*. en. URL: [https://www.microscope.healthcare.nikon.com/en\\_AOM/products/super-resolution-microscopes/n-storm-super-resolution/the-principle-of-stochastic-optical-reconstruction-microscopy](https://www.microscope.healthcare.nikon.com/en_AOM/products/super-resolution-microscopes/n-storm-super-resolution/the-principle-of-stochastic-optical-reconstruction-microscopy).
- [9] Thermo Fisher Scientific. *Alexa Fluor 647 Dye*. en. URL: <https://www.thermofisher.com/ee/en/home/life-science/cell-analysis/fluorophores/alexafuor-647.html>.
- [10] Nicolas Olivier et al. “Simple buffers for 3D STORM microscopy”. EN. In: *Biomedical Optics Express* 4.6 (June 2013). Publisher: Optica Publishing Group, pp. 885–899. DOI: 10.1364/BOE.4.000885.
- [11] Russell E. Thompson, Daniel R. Larson, and Watt W. Webb. “Precise Nanometer Localization Analysis for Individual Fluorescent Probes”. English. In: *Biophysical Journal* 82.5 (May 2002). Publisher: Elsevier, pp. 2775–2783. DOI: 10.1016/S0006-3495(02)75618-X.
- [12] Bo Huang et al. “Three-dimensional Super-resolution Imaging by Stochastic Optical Reconstruction Microscopy”. In: *Science (New York, N.Y.)* 319.5864 (Feb. 2008), pp. 810–813. DOI: 10.1126/science.1153529.

- [13] Marijn Siemons et al. “Comparing strategies for deep astigmatism-based single-molecule localization microscopy”. In: *Biomedical Optics Express* 11.2 (Jan. 2020), pp. 735–751. DOI: 10.1364/BOE.382023.
- [14] Yoonsuk Hyun and Doory Kim. “Development of Deep-Learning-Based Single-Molecule Localization Image Analysis”. en. In: *International Journal of Molecular Sciences* 23.13 (Jan. 2022). Number: 13 Publisher: Multidisciplinary Digital Publishing Institute, p. 6896. DOI: 10.3390/ijms23136896.
- [15] Magdalena C. Schneider et al. “Interactive simulation and visualization of point spread functions in single molecule imaging”. In: *Optics Communications* 560 (June 2024), p. 130463. DOI: 10.1016/j.optcom.2024.130463.
- [16] Kenneth N. Fish. “Total Internal Reflection Fluorescence (TIRF) Microscopy”. In: *Current protocols* 2.8 (Aug. 2022), e517. DOI: 10.1002/cpz1.517.
- [17] Boris Ferdman et al. “VIPR: vectorial implementation of phase retrieval for fast and accurate microscopic pixel-wise pupil estimation”. EN. In: *Optics Express* 28.7 (Mar. 2020). Publisher: Optica Publishing Group, pp. 10179–10198. DOI: 10.1364/OE.388248.
- [18] Yuya Nakatani et al. “Long axial-range double-helix point spread functions for 3D volumetric super-resolution imaging”. In: *bioRxiv* (Aug. 2024), p. 2024.07.31.605907. DOI: 10.1101/2024.07.31.605907.
- [19] David Baddeley, Mark B. Cannell, and Christian Soeller. “Three-dimensional sub-100 nm super-resolution imaging of biological samples using a phase ramp in the objective pupil”. en. In: *Nano Research* 4.6 (June 2011), pp. 589–598. DOI: 10.1007/s12274-011-0115-z.
- [20] Marijn E. Siemons, Lukas C. Kapitein, and Sjoerd Stallinga. “Axial accuracy in localization microscopy with 3D point spread function engineering”. EN. In: *Optics Express* 30.16 (Aug. 2022). Publisher: Optica Publishing Group, pp. 28290–28300. DOI: 10.1364/OE.461750.
- [21] Wesley R. Legant et al. “High-density three-dimensional localization microscopy across large volumes”. en. In: *Nature Methods* 13.4 (Apr. 2016). Publisher: Nature Publishing Group, pp. 359–365. DOI: 10.1038/nmeth.3797.
- [22] M. Laasmaa, M. Vendelin, and P. Peterson. “Application of regularized Richardson–Lucy algorithm for deconvolution of confocal microscopy images”. en. In: *Journal of Microscopy* 243.2 (2011). \_eprint: <https://onlinelibrary.wiley.com/doi/pdf/10.1111/j.1365-2818.2011.03486.x>, pp. 124–140. DOI: 10.1111/j.1365-2818.2011.03486.x.
- [23] Martin Ovesný et al. “ThunderSTORM: a comprehensive ImageJ plug-in for PALM and STORM data analysis and super-resolution imaging”. In: *Bioinformatics* 30.16 (Aug. 2014), pp. 2389–2390. DOI: 10.1093/bioinformatics/btu202.

## Appendices

### Appendix 1 - Non-exclusive licence for reproduction and publication of a graduation thesis<sup>1</sup>

Annex  
to Rector's directive No 1-8/17 of 7 April 2020

I Marten Pärj

1. grant Tallinn University of Technology free licence (non-exclusive licence) for my thesis "*Implementing 3D Imaging in Single Molecule Localization Microscopy with Astigmatism*", supervised by Martin Laasmaa,
  - 1.1 to be reproduced for the purposes of preservation and electronic publication of the graduation thesis, incl. to be entered in the digital collection of the library of Tallinn University of Technology until expiry of the term of copyright;
  - 1.2 to be published via the web of Tallinn University of Technology, incl. to be entered in the digital collection of the library of Tallinn University of Technology until expiry of the term of copyright.
2. I am aware that the author also retains the rights specified in clause 1 of the non-exclusive licence.
3. I confirm that granting the non-exclusive licence does not infringe other persons' intellectual property rights, the rights arising from the Personal Data Protection Act or rights arising from other legislation.

21.05.2025

---

<sup>1</sup>The non-exclusive licence is not valid during the validity of access restriction indicated in the student's application for restriction on access to the graduation thesis that has been signed by the school's dean, except in case of the university's right to reproduce the thesis for preservation purposes only. If a graduation thesis is based on the joint creative activity of two or more persons and the co-author(s) has/have not granted, by the set deadline, the student defending his/her graduation thesis consent to reproduce and publish the graduation thesis in compliance with clauses 1.1 and 1.2 of the non-exclusive licence, the non-exclusive license shall not be valid for the period.